Truncating Tau Reveals Different Pathophysiological Actions of Oligomers in Single Neurons

Emily Hill[1*], Thomas K. Karikari[2], Juan Lantero-Rodriguez[2], Henrik Zetterberg[2,3,4,5], Kaj Blennow[2,3], Magnus J Richardson[6], Mark J Wall[1*]

[1]School of Life Sciences, University of Warwick, Coventry CV4 7AL, United Kingdom

[2]Department of Psychiatry and Neurochemistry, Institute of Neuroscience and Physiology, University of Gothenburg, SE-43180 Mölndal, Sweden.

[3]Clinical Neurochemistry Laboratory, Sahlgrenska University Hospital, SE-43180 Mölndal, Sweden.

[4]UK Dementia Research Institute at UCL, London WC1E 6BT, United Kingdom

[5]Department of Neurodegenerative Disease, UCL Institute of Neurology, London WC1E 6BT, United Kingdom

[6]Institute of Mathematics, University of Warwick, Coventry CV4 7AL, United Kingdom

*Authors for correspondence: Emily Hill E.hill.2@warwick.ac.uk and Mark Wall Mark.wall@warwick.ac.uk

Abstract

Tau protein is involved in maintaining neuronal structure. In Alzheimer's disease, small numbers of tau molecules can aggregate to forms oligomers. However, how these oligomers produce changes in neuronal function remains unclear. Previously, oligomers made from full-length human tau were found to have multiple effects on neuronal properties. Here we have cut the tau molecule into two parts: the first 123 amino acids and the remaining 124-441 amino acids. These truncated tau molecules had specific effects on neuronal properties, allowing us to assign the actions of full-length tau to different regions of the molecule. We identified one key target for the effects of tau, the voltage gated sodium channel, which could account for the effects of tau on the action potential. By truncating the tau molecule, we have probed the mechanisms that underlie tau dysfunction, and this increased understanding of tau's pathological actions, will build towards developing future tau-targeting therapies.

36

37

38

39

40   **Introduction**

41   Tau is a microtubule-associated protein which can modify neuronal morphology, vesicle transport and
42   trafficking (1,2). Tau dysfunction contributes to diseases, termed tauopathies, either as the primary
43   causative agent (e.g., Pick's disease) or as a component of the neuropathology (e.g., Alzheimer's
44   disease, AD). Tauopathies have varying histopathological and clinical presentations and are often
45   distinguished by the ultrastructure of the tau aggregates (3,4). In AD, abnormally phosphorylated tau
46   dissociates from microtubules and aggregates to form oligomers and fibrils, accumulating in the
47   soma-dendritic compartment (5). Tau can further aggregate to form neurofibrillary tangles (NFTs),
48   whose abundance correlates with disease progression (6,7). However, it appears that the soluble tau
49   oligomers (oTau) are the most bioactive, in terms of disrupting neuronal function. Indeed, the toxic
50   effects of tau oligomers can occur in the absence of NFT pathology (8–10). Although the toxicity of
51   oTau is now well established, the mechanistic basis of oTau actions on neuronal function are poorly
52   understood.

53   Electrophysiological studies have revealed several pathological mechanisms for the actions of full
54   length (FL) oTau, including alterations in neuronal excitability and short- and long-term synaptic
55   plasticity (11–14). Viral introduction and transgenic models are commonly used to explore the roles of
56   oTau in pathology (8–10). While these methods generate valuable data, they provide little information
57   on the concentration and structural conformations of oTau that are responsible for the neurotoxic
58   effects. For other approaches, such as the extracellular application of oTau to tissue or cell cultures
59   (15–17), cellular uptake may be the limiting step, reducing the observed toxicity. Moreover, it is not
60   possible to target oligomers to either pre- or post-synaptic neurons and homeostatic adaptation may
61   occur.

62   To address these limitations, whole-cell patch-clamp recording has recently been used to introduce
63   oTau into single neurons and has enabled specific targeting to either pre- or post-synaptic cells
64   (11,18). This approach only requires small amounts of oligomers, each cell acts as its own control and
65   electrophysiological alterations can be observed in real time. Furthermore, direct comparisons can be
66   made between different concentrations and structural conformations of the oTau introduced
67   (11,19,20).

68   Previously, full-length (FL, prepared from full-length human tau 1-441) oTau (44-444 nM) was shown
69   to modify the excitability (as measured by a change in firing rate), input resistance and action potential

70   waveform of CA1 pyramidal neurons (11). We hypothesized that specific truncations of the tau

71   molecule may allow these various effects to be dissected apart, identifying the underlying

72   mechanisms and which parts of the molecule cause which effect. We therefore created truncated

73   versions of tau informed by a physiologically relevant truncation at amino acid 123 that was recently

74   discovered in AD patients (21). We used oligomers formed from tau lacking the N-terminal region (aa

75   124-444; C^{FRAG}) and soluble aggregates of the non-oligomer forming N-terminal fragment (aa 1-123;

76   N^{FRAG}). Using these tau constructs, we have identified specific mechanisms underlying the changes to

77   excitability (firing rate), whole-cell conductance and action potential waveform.

78   **Results**

79   **Structural characterisation of the tau samples**

80   A validated method was used to generate non-fibrillar soluble tau aggregates without the use of

81   aggregation-inducing factors such as heparin (11,22,23) Incubating all three tau samples at room

82   temperature overnight led to the formation of small soluble aggregates (FL oligomers, C^{FRAG}

83   oligomers, N^{FRAG} soluble aggregates; Figure 1A), as shown by negative-stain transmission electron

84   microscopy (TEM) for both truncations and the full-length version of tau. However, there are likely to

85   be structural differences in the aggregate conformers; C^{FRAG}-tau is more likely to form granular

86   shaped oligomeric aggregates similar to those of FL-oTau (Figure 1B and 11; 21, 22). Conversely,

87   N^{FRAG}-tau is more likely to form more amorphous, irregular-shaped, non-amyloidogenic aggregates, in

88   agreement with (24). For each variant, monomeric controls (incubated for the same duration but at 4

89   ˚C) did not form aggregates (Figure 1B).

90

91   **Removing the N-terminal region of tau (aa 1-123) abolishes the effects of tau on action**

92   **potential waveform and input resistance, but the increase in firing rate remains.**

93   We first compared the effects of C^{FRAG}-oTau (aa124-444) to FL-oTau (with vehicle as control). There

94   was no significant difference in the electrophysiological parameters of the recorded neurons

95   measured at time 0 (whole-cell breakthrough) between all 3 of the experimental conditions. Therefore,

96   the initial quality of recordings and neuronal properties were comparable. In control neurons, there

97   were no significant changes to any of the measured parameters across the duration of recordings (40

98   minutes, Figure 2; Table 1). There were also no changes to the resting membrane potential for any of

99   the experimental conditions across the duration of recordings (Figure 2A, B; Table 1). FL-oTau had

100   comparable effects to those previously reported in (11): increasing input resistance, increasing

101   neuronal firing rate (a correlate of neuronal excitability) and changing the action potential waveform

102   (reducing height, amplitude relative to baseline, and increasing width). These effects were specific to

103   oligomers, with monomeric FL-oTau having no significant effects (11) and are not the result of the tau

104   oligomers blocking the tip of the recording pipette, as a number of controls have previously been

105   carried out to eliminate this possibility (11,19,20).

106

107   The increase in firing rate induced by FL-oTau, was previously assumed to be the result of the

108   increase in input resistance (Figure 2C, D, E) as less current will be required to produce the same

109   voltage change. However, although C^{FRAG}-oTau had no significant effect on input resistance (Figure

110   2C), it still significantly increased the firing rate (induced by current injection) suggesting that the

111   effects on firing rate can occur independently of changes in input resistance (Figure 2C-E). In contrast

112   to FL-oTau, which in agreement with (11), significantly increased action potential width and decreased

113   action potential height, introduction of C^{FRAG}-oTau had no significant effects on the action potential

114   waveform (Figure 2D-G). Thus, loss of the first 123 amino acids from tau removes the effects on input

115   resistance and action potential waveform. These effects could either be a direct effect of the N-

116   terminal sequence or could result from a change in the structural conformation of the oligomers, which

117   could differ following truncation.

118   **A reduction in the rheobase current induced by C^{FRAG}-oTau is consistent with its effects on**

119   **firing rate.**

120   To evaluate the effects on neuronal excitability in more detail, we examined the rheobase (the

121   minimal current required to elicit an action potential). The rheobase was measured by injecting a

122   current ramp (see methods). There was no significant difference in the rheobase in control (vehicle)

123   vs FL or C^{FRAG} -oTau injected neurons at time 0 (Table 1, Figure 3). In control neurons, there was no

124   significant difference in the rheobase current over the duration of the recording. However, when either

125   FL or C^{FRAG} -oTau were introduced, the rheobase was significantly reduced (Table 1, Figure 3). This

126   is consistent with the observed increased in firing rate in response to fluctuating noisy current injection

127   (Figure 2F, G).

128

129   **C^{FRAG} tau oligomers reduce the current needed to elicit APs**

130   We hypothesized that the decrease in rheobase current might be due to a smaller difference between

131   the resting membrane potential and spike initiation threshold (value of membrane potential that needs

132   to be surpassed to fire an action potential). Since there is no change in resting membrane potential,

133   this could only occur if there was a hyperpolarising shift in spike initiation threshold. The dynamic IV

134   method (25–27) provides a protocol to accurately parameterise neurons including spike initiation

135   threshold (see methods). In (11), it was not possible to map changes in neuronal parameters over

136   time using the dynamic IV method, as it is not very effective if there are significant changes in the

137   action potential waveform. However, as C^{FRAG} -oTau has no effect on the action potential waveform, it

138   is possible to use this method to measure spike initiation threshold. There was no significant

139   difference between the spike initiation threshold in control neurons (vehicle) vs neurons receiving in

140   C^{FRAG}-oTau at 0 mins. In control neurons, there was no significant difference in spike initiation

141   threshold after 40 minutes (recording duration), whereas for neurons where C^{FRAG} -oTau was

142   introduced, spike initiation threshold was significantly hyperpolarised. Although the reduction in spike

143   initiation threshold was only ~4 mV, across a network this would cause a large shift in excitability. We

144   also noted an increase in spike onset sharpness, which is a measure of how narrow the voltage range

145   within which a spike starts to initiate, as well as how sharply the spike begins to rise (sharper DIV

146   curve). In control neurons, there was no significant difference in spike onset over the duration of the

147   recording, whereas for neurons where C^{FRAG} -oTau was introduced, the onset was increased (steeper,

148   reflecting increased excitability). It can be noted that though the spike-onset range was broader at 40

4

149   mins, this change (unlike for the spike threshold parameter VT) had no significant effect on the firing

150   rate (see Figure 4D).

151

152   **N^{FRAG}-tau aggregates generate a rapid increase in input resistance and change action potential**

153   **waveform.**

154   As C^{FRAG} -oTau did not replicate the changes to input resistance and action potential waveform

155   observed with FL oTau, we next introduced N^{FRAG}-tau (aa1-123) and measured changes in neuronal

156   parameters to determine if this fragment of tau could produce these effects. Unexpectedly, in

157   preliminary experiments we observed a large increase in input resistance induced by N^{FRAG} -tau within

158   the first 5 minutes of recording (Figure 5A). This effect occurred without a change in the bridge

159   balance confirming that the tau fragment is not blocking the patch pipette tip (Supplementary Figure

160   8). It has previously been shown that FL-oTau neither aggregates in the end of the pipette tip nor

161   impedes voltage measurements through re-patching experiments (11). However, this rapid change

162   could be due to N^{FRAG}-tau forming aggregates close to the introduction site in the soma and reducing

163   the apparent electrotonic size of the soma. By fitting the voltage step (exponential) we extracted the

164   time constant and used this to calculate cellular capacitance using the following equation:

165

$$Time\ constant\ (T) = Input\ resistance\ (R_{in})\ x\ Capacitance\ (C) \qquad Eq.\,1$$

166

167   By 5 mins, the time constant was significantly reduced, reflecting a change in whole-cell capacitance.

168   To test the possibility that this rapid change to whole-cell resistance and capacitance could be due to

169   the aggregation of the N^{FRAG}-tau in the soma impeding current flow, we performed a subset of

170   experiments where two simultaneous whole-cell patch clamp recordings were made from the soma of

171   the same CA1 pyramidal neuron (Figure 5 B-F, see methods). We injected current only via pipette 1

172   and then measured the ratio of the voltage responses in pipette 1 and pipette 2 (voltage pipette 2/

173   voltage pipette 1) (Figure 5C). We hypothesised that if N^{FRAG}-tau was injected via pipette 1, there will

174   be an increase in the whole cell resistance, less current will leak out from the neuron and thus the

175   voltage response measured from both pipettes will be increased without a change in the ratio. If

176   however the N^{FRAG}-tau aggregates in the soma and interferes with the current flow between the

177   pipettes then the ratio of the voltage response between the pipettes will be reduced as less current

178   will reach pipette 2.

179

180   A 200 pA (1s) hyperpolarising step was only injected via pipette (1.) and voltage responses were

181   measured from both pipettes (Figure 5C, pipettes 1. and 2.). As the current needs to travel from

182   pipette 1 to pipette 2, the voltage response was always slightly smaller in pipette 2 than in pipette 1. In

183   cells where both pipettes contained vehicle, there was no change in the relative amplitude of the

184   voltage responses between 0 mins (whole-cell breakthrough) and 5 mins (Figure 5D). However, when

185   N^{FRAG} -oTau was introduced via pipette 1, there was a large increase in the voltage response

186   measured by pipette 1 as a result of the increase in cell resistance (Figure 5E) . However, this was

187   not reflected by an increase in the amplitude of the voltage step measured by pipette 2 (Figure 5E, F).

188 Thus, the ratio of voltage pipette 2/ voltage pipette 1) was significantly reduced (Figure 5E, F). This

189 result is consistent with N^{FRAG}-tau accumulating in the soma, impeding the flow of current between

190 the two pipettes, resulting in an 'increase in the apparent input resistance and a decrease in the

191 observed capacitance due to the cell appearing electronically smaller.

192

193 **N^{FRAG} Tau-mediated changes to action-potential waveform are independent of aggregation**

194 **state**

195 We have demonstrated that the FL-oTau mediated increase in input resistance and changes to the

196 action potential waveform occurred at later time points than we observed with N^{FRAG}-tau. This may be

197 because the FL o-Tau does not aggregate as rapidly as N^{FRAG}-tau and thus takes longer to have its

198 effects. To examine the effects of N^{FRAG}-tau in more detail we used a lower concentration (133 nM)

199 which may mimic the slower effects of FL-oTau. There were no effects of 133 nM N^{FRAG}-tau on resting

200 membrane potential, input resistance, firing rate or the rheobase current (Figures 6A-D). However,

201 there were significant changes to the action potential waveform (increased width and decreased

202 height, Figures 6E-G). These changes were similar to that observed with FL-oTau in this study and in

203 (11). This was unexpected as the N-terminal fragment would be predicted to form structurally different

204 aggregates to those formed by FL tau oligomers. We repeated the experiments with the monomeric

205 version of N^{FRAG}-tau and found no changes in resting membrane potential, input resistance, firing rate

206 or rheobase current (Figure 6A-D). However, a comparable change to the action potential waveform

207 was observed to the aggregated form of the fragment (Figure 6E-G). Given that the oTau-induced

208 changes to action potential waveform that occur with full length tau (11) also occurred with the N-

209 terminal fragment (N^{FRAG}-Tau), both as a monomer and as an oligomer, it is likely that there is a

210 sequence within the 1-123 amino acid region that directly interacts with a cellular component, rather

211 than being an effect of the quaternary structure of the aggregates.

212

213 **FL-oTau alters somatic voltage gated sodium channel half activation and slows the rate of**

214 **activation**

215 Having demonstrated changes to the action potential waveform and a hyperpolarising shift in spike

216 threshold, making the neurons more excitable, we next investigated whether these changes were

217 mediated by interactions of tau with voltage gated sodium channels. FL-oTau (444 nM) was used in

218 these experiments to evaluate whether both or either of its observed effects (on action potential

219 waveform and firing rate) could be a result of an interaction with sodium (NaV) channels. FL-oTau

220 was compared against control (vehicle). Recording sodium channel currents in hippocampal neurons

221 in acute brain slices is challenging due to problems with space clamp, given the size of the neurons

222 and the large amplitude and speed of the currents. One way to effectively clamp the currents, is to

223 electronically isolate the soma. We followed the protocol outlined in (28), using a short depolarising

224 pre-pulse to inactivate the axonal sodium channels, leaving only the somatic channels to be activated

225 (see methods). It was then possible to achieve reasonable voltage clamp (Figure 7A). Normalised

226 conductance's were plotted against voltage and fitted with a Boltzmann function. The fit (Figure 7B, C)

227 was used to extract the half activation voltage and the rate constant of activation (indicative of the rate

6

228 of rise in conductance relative to change in voltage). The half activation was stable in control
229 recordings, whereas in neurons that had FL-oTau 444 nM introduced, by 20 minutes the half
230 activation had shifted significantly in a negative direction to activate ~ 4mV earlier, reflective of an
231 increase in excitability (Figure 7). This could account for the change in spike threshold that was
232 observed with C^{FRAG} oTau. We also extracted the rate constant of activation; a smaller rate constant
233 would indicate a steeper relationship between conductance and voltage. The rate constant of
234 activation was stable in control, whereas in neurons that had FL-oTau introduced, by 20 minutes it
235 had increased significantly (shallower slope, reflective of a flatter relationship to voltage). This change
236 could explain the slowing of the action potential rising phase observed in (11) and in this study.

237

238 We then implemented a simplified model of the neuronal action potential with general applicability
239 (29) to evaluate whether the conductance changes mediated by FL-oTau could feasibly underly the
240 changes we observed in action potential waveform. Our experimental voltage gated sodium current
241 recordings showed that FL-oTau mediates a reduction of $\bar{g}_{Na}$ to by two thirds of the value at 0
242 minutes after 20 minutes (7F-I). Therefore, we first simulated an action potential with $\bar{g}_{Na} =$
243 $120 \ mS/cm^2$ (28, Figure 7J, red) and then again with $\bar{g}_{Na} = 40 \ mS/cm^2$ (Figure 7J, red trace). We
244 found that this reduction in maximal conductance matches the experimental phenotype well (in
245 particular the changes in action potential amplitude and speed of rise to threshold; Figure 7K).

246

247 **Discussion**
248 In Alzheimer's disease (AD) and in other tauopathies, tau aggregates into small soluble toxic
249 oligomers,
250 a process that precedes the formation of large insoluble aggregates (NFTs). In AD, NFTs and
251 amyloid-
252 β plaques are the characteristic hallmarks of the disease with post-mortem confirmation of both NFTs
253 and plaques required for definitive diagnosis (6,7,30). Many studies have shown that the small soluble
254 aggregates (oligomers) formed early in the aggregation pathway are much more bioactive than NFTs
255 pathology (8–10). These findings have led to the targeting of oligomers to reduce tau cytotoxicity in
256 disease models and in AD patients. However, the mechanisms of how these oligomers produce
257 neuronal dysfunction are still not fully defined. Here, we have used specific truncations to dissect
258 apart the actions of full length (FL) -oTau. We have used oligomers formed from N-terminal truncated
259 tau (aa 124-444; C^{FRAG}) and soluble aggregates of the non-oligomer forming N-terminal fragment (aa
260 1-123; N^{FRAG}).

261

262 It is conceivable that some of the changes in electrophysiological properties that we have observed
263 could result from tau oligomers blocking the tip of the patch pipette and increasing series resistance.
264 In particular the changes in action potential amplitude and waveform kinetics. In previous studies
265 (11,19,20) and in this study we have carried out a number of control experiments that have allowed us
266 to reject this possibility. These controls include monitoring of series resistance throughout recordings
267 and adjusting the bridge balance as required, introducing large concentrations of a control protein

268   (BSA, 20 μM vs 44-144 nM) into neurons and observing no change in series resistance, repatching
269   neurons (with vehicle in the patch solution) which had been injected with tau oligomers and showing
270   that the changes in action potential waveform persisted (11). We have subsequently checked that the
271   open tip resistance of patch pipettes does not change over time (as a result of clogging with tau
272   oligomers). In this study we have found that it is the smallest fragment of the tau oligomer that has
273   the greatest effects on action waveform, which is the opposite to what would be expected if it was just
274   the tau oligomers non-specifically blocking the pipette tip. We have also previously investigated the
275   effects of alpha-synuclein oligomers on neuronal properties by introducing them via the patch pipette
276   (19). These oligomers are much larger than the tau oligomers but had no effect on the action potential
277   amplitude or waveform kinetics (19).

278

279   The N-terminal truncation (C^{FRAG}) at position 123, has been identified as a major N-terminal cleavage
280   site in tau found in human CSF (21) and a truncated tau construct at a nearby position has been used
281   to study effects on synaptic transmission (31). We found that C^{FRAG}-oTau did not replicate the effects
282   on action potential kinetics or input resistance that were observed with FL-oTau but did still increase
283   firing rate. This firing rate increase is mediated by a reduction in the minimum current required to elicit
284   an action potential. Using the dynamic IV protocol we found that C^{FRAG}-oTau reduces spike threshold
285   by ~ 4mV. Since there was no change in the resting membrane potential, the difference between
286   spike threshold and resting potential was reduced, increasing the likelihood of firing. A
287   hyperpolarisation of spike threshold (~ 3 mV) has also been previously reported in Tau35 transgenic
288   mice (32). To confirm our observation further, the parameters extracted from the dynamic IV curve at
289   0 minutes were used to simulate voltage responses using the exponential integrate and fire model
290   (25–27,33). The control firing rate was comparable to experimental values. A reduction in the spike
291   threshold by the experimentally observed reduction (4 mV), was sufficient to increase the firing rate to
292   comparable experimental values with C^{FRAG} oTau. Thus, it is feasible for a change in spike threshold
293   (without any change in input resistance) to mediate the observed changes in firing rate (a correlate of
294   excitability) by C^{FRAG} oTau.

295

296   We then investigated the tau fragment that was removed to generate C^{FRAG} (aa 1-123; N^{FRAG}). This
297   fragment (N^{FRAG}) makes up a large proportion of N-terminal tau species found in human CSF, and it
298   could therefore represent a marker of tau metabolism (21). N^{FRAG} does form aggregates but these are
299   likely to differ from the FL-oTau oligomers. When N^{FRAG} was introduced into neurons at equivalent
300   concentrations to FL-oTau (444 nM), it produced a rapid increase in input resistance, reduced action
301   potential amplitude and slowed action potential kinetics. These effects occurred within ~ 5 minutes.
302   Through measurements of the cell time constant we found that the apparent capacitance was
303   significantly decreased. This led us to hypothesise that N^{FRAG} was inferring with current flow, making
304   the neuron electrotonically smaller. By making simultaneous dual patch clamp recordings from the
305   soma of a single neuron, we found that although input resistance was significantly increased, the
306   current flow between the electrodes had significantly decreased. This is consistent with N^{FRAG} tau
307   aggregating in the soma and impeding current flow across the cell.

308

309   Introducing N^{FRAG} at lower concentrations (133 nM) changed action potential height and width without

310   increasing input resistance or changing cell capacitance. Thus, the changes in action potential

311   waveform were not simply due to increased filtering. Surprisingly, N^{FRAG} monomers produced

312   comparable changes to APs. Thus, the effects of N^{FRAG} are unrelated to its quaternary structure and

313   instead maybe associated with a specific sequence within N^{FRAG} and FL-oTau. Given the nature of the

314   changes in action potential waveform we hypothesised that tau might be interacting with voltage-

315   gated sodium channels and altering their function.

316

317   Changes in action potential kinetics and amplitude can readily be measured using whole cell current

318   clamp (29). However, recording the underlying sodium currents from neurons in slices using voltage

319   clamp is challenging due to poor space clamp and the large amplitude and rapid rise of currents

320   (34,35). A large proportion of sodium channels are clustered in the axon initial segment (AIS, 35–37),

321   and their activation voltage can differ from that at the soma (37,39). Thus, these electrotonically

322   remote sodium channels will generate unclamped currents, which prevent the measurement of

323   controlled responses. To counteract this problem, many studies measurements of sodium channel

324   currents are performed using dissociated or cultured neurons or in cell lines. However, these are less

325   relevant physiologically relevant because the distribution, density and expression pattern of channels

326   will be different from what is found in situ. An alternative approach is to use nucleated patches, which

327   would provide a better voltage clamp, but the small volume of the patch may alter the amount of tau

328   reaching the channels. It would therefore be difficult to accurately titrate the concentration of tau to

329   make it compatible with the experiments done in whole cells. We have therefore adapted a protocol

330   (28) to make controlled voltage clamp recordings in acute slices. A pre-pulse elicits an uncontrolled

331   voltage response which activates axonal but not somatic sodium channels. As the axonal channels

332   are inactivated, only the sodium channels in the soma contribute to the actual recorded current,

333   allowing for finely controlled voltage clamp of the sodium currents. This protocol also required a

334   number of other steps to produce clamp of isolated sodium channel currents including changing the

335   Na^+ concentration inside and outside of the neuron, performing recordings at room temperature and

336   replacing the calcium ions with cobalt to block voltage gated calcium channels (40). Those recordings

337   in which Na^+ channels were not adequately clamped were readily identifiable and excluded from

338   analysis (Supplementary Figure 7).

339

340   There are four subtypes of voltage-gated sodium channel present in the mammalian central nervous

341   system, NaV 1.1,1.2,1.3,1.6 (41). At the AIS of CA1 pyramidal neurons, NaV1.1, NaV1.2, and NaV1.6

342   channels have been identified (42–44). NaV1.6 is highly abundant and has a more hyperpolarized

343   voltage of activation compared with the other sodium channel isoforms, contributing to the lower

344   activation threshold (38). The sodium channels in the AIS probably contribute little to the clamped

345   currents and this is a possible limitation of the technique. However, NaV1.6 is also expressed in the

346   soma, 10 although at less abundance than at the AIS (45).

347

348   FL-oTau had three effects on sodium channel currents: Firstly, the half activation was reduced,

349   reflecting the increase in neuronal excitability, consistent with the effects of C^{FRAG}-oTau. Secondly,

350   the rate of activation was reduced underlying the slower action potential rise, consistent with the

351   effects of N^{FRAG}-tau. Finally, FL-oTau reduced $\bar{g}_{Na}$ (maximum sodium conductance) by ~ two thirds.

352   To investigate the effects this would have on the AP, we implemented a simplified action potential

353   model (29). Reducing $\bar{g}_{Na}$ had effects that matched the experimental data (reduced action potential

354   amplitude and change to threshold). Thus, this reduction in conductance could account for the

355   changes that we observe experimentally.

356   From unnormalized conductance plots, we noticed that the rate of conductance increase appeared

357   faster for FL-oTau despite $\bar{g}_{Na}$ being reduced (Figure 7I). We therefore modelled the initial rise of the

358   sodium current using the same approach (33) used to derive the original model:

359

360
$$I_{Na} = (E_{Na} - E_{rest}) * g1 * e^{\left(\frac{V-V1}{\Delta T}\right)} \qquad Eq.\,2$$

361

362   Where $g1$ is 1 nS and V1 is the voltage where the conductance is 1 nS. For FL-oTau introduced cells,

363   ΔT was calculated to be stable ~2.65 mV for 0 mins and 20 mins but $V1$ varied over time. At 0 mins,

364     $V1$ = -32 mV and by 20 mins, $V1$ = -36 mV, demonstrating that a sodium conductance of 1 nS is

365   achieved at a much lower voltage, thus the cell is more excitable (despite the peak sodium

366   conductance being lower overall, Figure 7I). In the EIF model, the sodium current is modelled as:

367

$$\Delta T * gL * e^{\left(\frac{V-VT}{\Delta T}\right)} \qquad Eq.\,3$$

368

369   and comparing this with the equation for I_{Na} we get:
370

371
$$VT = V1 + \Delta T * \log\left(gL * \frac{\Delta T}{g1} * (E_{Na} - E_{rest})\right) \qquad Eq.\,4$$

372
373   Empirically, the first term V_1 on the right-hand-side is dependent on parameters that change between

374   0 mins and 40 mins, whereas the second term does not change significantly between these time

375   steps. Hence the modelling predicts that the change in the action-potential threshold parameter V_T is

376   largely due to changes in V_1 which is the voltage at which the sodium current is 1nS. The I_{Na}

377   experiments predict that the difference in VT at 0 and 40 mins is 4 mV, which fits exactly with the

378   excitability phenotype modelled using C^{FRAG}. Despite the differences in temperature for these

379   recordings, these two independent methodologies further support that the tau-mediated shift in

380   excitability comes from a lowering of the action-potential threshold (rather than input resistance

381   changes) and that this change is mediated via a lowering of the sodium current activation. In future

382   studies, it would be interesting to investigate the effects of tau oligomers on sodium channel

383   inactivation. If the inactivation curve is negatively shifted by tau oligomers, this would increase the

384   fraction of sodium channels inactivated at the resting membrane potential and this could also

385   contribute to the reduction in maximal conductance.

10

386

387 It is surprising to note that the difference in sodium conductance at 0 minutes and 20 minutes with FL-
388 oTau is dependent on voltage, at low voltages the conductance is bigger at 20 mins in FL-oTau but at
389 high voltages it is lower at 20 mins in o-Tau, thus, the effect is non-monotonic. Globally it appears that
390 there is a lower maximal Na conductance at 20 mins (and therefore action potential height is
391 reduced), but there is a small region at lower voltages where the conductance is higher for FL-oTau
392 which means the model is more excitable. This means the profile of the I_{Na} activation has been
393 changed by oTau; it is not just an issue of different maximal conductance magnitudes.

394

395 The simplest explanation for these changes to sodium conductance is that a specific N^{FRAG}-tau
396 sequence binds to the sodium channel. The mammalian sodium channel is a molecular complex of an
397 ~2000 amino acid α-subunit, which contains the pore and drug interaction sites, and smaller β-
398 subunits,
399 which modulate membrane expression (46,47). The α-subunit is divided into 4 domains each with 6
400 segments (S1-S6). S1-4 form the voltage sensing domain (48) and S5-6 form the pore forming
401 domain. Upon depolarisation, S6 segments move leading to channel opening via the P-loop between
402 S5 and S6 which forms the channel pore (41,49). The S4 segments contain a high proportion of
403 positively charged amino acid residues, making it responsive to changes in membrane potential (50).
404 It is interesting to speculate on where the tau oligomers could bind to sodium channels, changing the
405 coupling between depolarisation and pore opening. Many studies have shown that changes in the S4
406 segments, associated linkers and cytoplasmic loops can all change the activation of the channels
407 (41,49).

408

409 This work has shown that by modifying the tau molecule it is possible to dissect apart the multiple
410 effects it has on neuronal function (Table 2) and identify the molecular targets that tau might bind to.
411 This not only provides information about the mechanisms of action of tau but also raises interesting
412 possibilities. Since the truncations used in this study have been found in the CSF of AD patients, then
413 the effects of tau will depend on the mixture of these molecules inside neurons. Thus, if tau is
414 primarily present as the C^{FRAG} then it will affect excitability and not change action potential waveform.
415 However, if the N^{FRAG} accumulates in the soma it will have large effects on neuronal integration and
416 action potential waveform. It wolud also be interesting to identify whether these effects are specific to
417 specific sodium channel isoforms, and therefore could effect some neurons more than others
418 depending on the isofroms present.

419

420 **Methods**

421 **Recombinant production of FL and tau fragments**

422 Constructs: FL tau (amino acids 1-441 of tau 2N4R; Uniprot ID P10636-8), as well as the amino acids
423 1-123 (C^{FRAG}) and 124-441 (N^{FRAG}) variants of this protein were recombinantly produced in *E. coli.*
424 The different fragments were PCR amplified using custom designed primers representing the 5' and
425 3' sequence respectively with Tau cDNA (RC213312, Origene) as template. The PCR fragment was

11

426   cloned directly into pET_SUMO, a 6XHis tag and SUMO protein expression plasmid (Invitrogen), with
427   a TA cloning site. Constructs were sequenced and transformed into E. coli BL21 (DE3) for
428   expression.

429   SUMO fusion protein expression: E.coli BL21 (DE3) containing the sequence-confirmed plasmid
430   constructs were incubated overnight in 20 ml Luria Bertani media with Kanamycin at a concentration
431   of 50 μg/ml. The next morning, the turbid culture was used to inoculate 1L of Luria Bertani media with
432   Kanamycin (50 μg/ml) at +37°C and when OD600 reached 0.5-0.7, protein expression was induced
433   with 1.0 mM IPTG o/n at +26-28°C. BL21 (DE3) cells overexpressing tau forms were harvested by
434   centrifugation at 7000 rpm for 20' at +4°C and the pellet stored at -20°C.

435   Purification: The pellet was resuspended in 5ml lysis buffer (20 mM Tris, 150 mM NaCl, 1% NP40 pH
436   7.5, plus a tablet of protease inhibitor cocktail from Roche) per mg of cell pellet and incubated at room
437   temperature for 30 min. The lysate was centrifuged for 20 min at 17,000×g, 4 °C and the supernatant
438   collected. The protein extract was added to Ni-NTA agarose (Novex) equilibrated with 10 mM
439   imidazole in 1x Native buffer and incubated with rotation at +4°C for 1h. Ni-NTA agarose was washed
440   with 1x Native buffer + 20 mM imidazole and 6xHis-SUMO-tau fusion protein was eluted with 250 mM
441   imidazole in 1x Native buffer. Purified fusion protein was dialysed against 50 mM Tris, 150 mM NaCl,
442   pH 8.0 and protein concentration was determined with BCA.

443   SUMO-tau fusion protein (2 mg) was cleaved by +4°C overnight incubation in 50 μg SENP-1 SUMO
444   protease in 50 mM Tris, 150 mM NaCl, 1 mM DTT. After cleavage, 6xHis-tag and His-tagged SUMO
445   protease was bound to Ni-NTA agarose, the flowthrough containing tag-free tau was collected and
446   any residual bound Tau protein was eluted with imidazole gradient, starting at 20 mM. Fractions
447   containing Tau protein were collected and dialyzed against PBS. If needed, protein was concentrated
448   using AmiconUltra4. Polishing of the tag-free tau protein variants to remove truncates and aggregates
449   was performed by size exclusion chromatography (51). We used a Superdex S200 10/300 GL column
450   (GE Healthcare) running on an Ethan LC system (GE Healthcare), with the running buffer being 1×
451   PBS pH 7.4 (2x PBS for tau1-123). The following molecular weight markers from Sigma (#MWGF70-
452   1KT) were used to estimate the elution volumes of the proteins of interest: blue dextran (2000 kDa;
453   void volume), bovine serum albumin (66 kDa), carbonic anhydrase (29 kDa), cytochrome C (12.4
454   kDa), and aprotinin (6.5 kDa). Each tau variant was purified in a two-step process; 1ml fractions from
455   the first size exclusion chromatography were analysed by gel chromatography followed by Western
456   blotting with specific tau antibodies to select high-protein fractions for further processing. Selected
457   high-yield fractions were pooled and concentrated using ultrafiltration devices of appropriate
458   molecular weight cut-offs from Amicon (51).
459

460   **Preparing of tau oligomers**
461   To ensure the use of equal concentrations of the tau variants, molar concentrations were estimated
462   using molecular weights specific to each tau construct sequence. Oligomers were prepared by
463   overnight incubation of identical concentrations of each protein construct in 1X PBS at room

12

464   temperature without shaking, a method validated (22). Monomers were treated similarly but were

465   incubated at 4 ˚C overnight. The samples were immediately dry-frozen by dipping into dry ice mixed

466   with ethanol and stored at -80 ˚C until use. Oligomer concentrations were expressed in equivalence of

467   starting monomer concentrations.

468   **Transmission electron microscopy**

469   Formvar/carbon-coated 300-mesh copper grids (#S162, Agar Scientific) were glow-discharged using

470   the ELMO system from Cordouan Technologies. Five microliters of labelled or unlabelled soluble tau

471   aggregate preparations were pipetted onto the grid and allowed to bind for 1 min. Excess samples

472   were removed with a strip of filter paper, and 5 µl of 2% uranyl acetate added for 1 min. After

473   removing the excess stain with a strip of filter paper, the grids were imaged using a JEOL-2100F

474   transmission electron microscope.

475   **Electrophysiology**

476   **Preparation of hippocampal brain slices**

477   All experiments were approved by the local Animals Welfare and Ethics Board (AWERB) at The

478   University of Warwick. C57/BL6 male mice (3-4 weeks of age) were killed by cervical dislocation and

479   decapitated in accordance with the United Kingdom Animals (Scientific Procedures) Act (1986).

480   Parasagittal hippocampal slices (350 µM) were cut with a Microm HM 650V microslicer in cold (2–

481   4°C) high Mg^{2+}, low Ca^{2+} aCSF (artificial CSF), composed of the following: 127 mM NaCl, 1.9 mM

482   KCl, 8 mM $MgCl_2$, 0.5 mM $CaCl_2$, 1.2 mM KH_2PO_4, 26 mM $NaHCO_3$, and 10 mM D-glucose (pH 7.4

483   when bubbled with 95% O2 and 5% CO_2, 300 mOsm). Following preparation, slices were left to

484   recover in recording aCSF (as above but with 1 mM $MgCl_2$ and 2 mM $CaCl_2$) at 34°C. Slices were

485   used within 1-8 hours after preparation.

486   **Whole-cell patch clamp recording from pyramidal cells**

487   A slice was transferred to the recording chamber, submerged and perfused (2–3 ml/min^{-1}) with aCSF

488   at 30 °C. Slices were visualized using IR-DIC optics with an Olympus BX151W microscope

489   (Scientifica) and a CCD camera (Hitachi). Whole-cell current-clamp recordings were made from

490   pyramidal cells in area CA1 of the hippocampus using patch pipettes (5–10 MΩ) manufactured from

491   thick-walled glass (Harvard Apparatus). Pyramidal cells were identified by their position in the slice,

492   morphology (from fluorescence imaging) and characteristics of the standard current−voltage

493   relationship. Voltage recordings were made using an Axon Multiclamp 700B amplifier (Molecular

494   Devices) and digitized at 20 kHz. Data acquisition and analysis were performed using pClamp 10

495   (Molecular Devices). Recordings from neurons that had a resting membrane potential of between –60

496   and –75 mV at whole-cell breakthrough were accepted for analysis. The bridge balance was

497   monitored throughout the experiments and any recordings where it changed by > 20 % were

498   discarded. Soluble tau aggregates were added to intracellular solution containing the following: 135

499   mM potassium gluconate, 7 mM NaCl, 10 mM HEPES, 0.5 mM EGTA, 10 mM phosphocreatine, 2

500   mM MgATP and 0.3 mM NaGTP (293 mOsm, pH 7.2) to give a final concentration of 444 nM (20

501   µg/ml tau) or 133 nM (6 µg/ml tau). These concentrations were chosen to align the study with

13

502   previously published findings (11). In control experiments, vehicle (PBS) was added instead of tau.

503   Intracellular solution was always filtered before adding tau aggregates to avoid any loss of tau in the

504   filter.

505   **Stimulation protocols**

506   To extract the electrophysiological properties of recorded neurons, both step, ramp and more

507   naturalistic, fluctuating currents were injected at 10-min intervals for a duration of the recordings as in

508   (11,19,20).

509

510   **Standard IV protocol**

511   The standard current−voltage relationship was constructed by injecting step currents from –200 pA

512   incrementing by either 50 or 100 pA (1 s) until a regular firing pattern was induced. A plot of step

513   current against voltage response around the resting potential was used to measure the input

514   resistance (gradient of the fitted line).

515

516   **Rheobase ramp protocol**

517   To evaluate the rheobase (minimum current needed to elicit an action potential; AP) a current ramp

518   was injected into neurons. From the baseline, a 100 ms ramp down by -50 pA, followed by a 900 ms

519   ramp up by 150 pA, then a step back down to baseline.

520

521   **Dynamic IV protocol**

522   The dynamic IV curve, defined by the average transmembrane current as a function of voltage during

523   naturalistic activity, can be used to efficiently parameterize neurons and generate reduced neural

524   models that accurately mimic the cellular response (20,22,25–27). Briefly, a current wave form,

525   designed to provoke naturalistic fluctuating voltages, was constructed using the summed numerical

526   output of two Ornstein–Uhlenbeck processes (52) with time constants τfast = 3 ms and τslow = 10 ms.

527   This current wave form, which mimics the background post-synaptic activity resulting from activation

528   of AMPA and GABA$_A$ receptor channels, is injected into cells and the resulting voltage recorded (a

529   fluctuating, naturalistic trace). The firing rate was measured from voltage traces evoked by injecting a

530   current wave form of the same gain for all recordings (firing rate ~2–3 Hz). APs were detected by a

531   manually set threshold and the interval between APs measured.

532   The dynamic transmembrane current (I_{ion}) can be calculated using:

533

534 $$I_{ion}(V,t) + I_{noise} = I_{inj}(t) - C\frac{dV}{dt} \qquad Eq.5$$

535

536   for which the injected current (I_{inj}) is known, the derivative (dV/dt) can be calculated from the

537   experimentally measured voltage and the capacitance (C) is attained from a minimum variance

538   procedure (26). A scatter plot of the transmembrane current against voltage illustrates the dynamic

539   relationship between the two, with the effects of weak background synaptic activity and other sources

540   of high-frequency variability being accounted for as intrinsic noise (I_{noise}) (26). Averaging the

14

541 transmembrane current in 1 mV bins removes the time dependence of I_{ion} (V,t) to yield the typical

542 ionic current and a particular voltage, and thus defines the dynamic I–V curve (I_{dyn}):

543

$$I_{dyn}(V) = Mean\ [I_{ion}(V,t)] \qquad Eq.6$$

544

545 It is well established that the exponential integrate-and-fire model (33) provides an excellent fit to the

546 dynamic I-V curve (25–27). The exponential integrate-and-fire (EIF) model is characterized by a

547 voltage forcing term F(V) that is related to the I_{dyn} as:

$$F(V) = \frac{-I_{dyn}(V)}{C} \qquad Eq.7$$

548

549 where the steady state forcing function F(V) for the EIF model is given as:

550

$$F(V) = \frac{1}{\tau}\left(E - V + \Delta_{\tau exp}\left(\frac{V - V_T}{\Delta_T}\right)\right) = -\frac{I_{dyn}(V)}{C} \qquad Eq.8$$

551 The dynamic curve fitted to the EIF model was used to extract four parameters: membrane time

552 constant (τ), resting potential (E), spike-initiation threshold (V_T) and spike-onset sharpness (Δ_T), which

553 describes the voltage range over which an action potential linitiates (20,25–27). Dynamic *I–V* curves

554 were constructed solely from the pre-spike voltage response (subthreshold and run up to spike) with

555 all data falling within a 200 ms window after each spike being excluded from analysis.

556 **Sodium channel current recordings**

557 To record sodium channel currents in isolation, the intracellular and extracellular solutions used were

558 modified from (28). The extracellular solution contained following (in mM): 124 NaCl, 25 NaHCO$_3$, 3

559 KCl, 1.5 CoCl$_2$, 1.0 MgSO$_4$, 0.5 NaH$_2$PO$_4$, and 30 D-glucose, equilibrated with 95% O$_2$ and 5% CO$_2$

560 (pH 7.4). Calcium chloride was replaced with cobalt chloride to block the voltage-gated calcium

561 channel currents. Experiments were performed at room temperature (~ 22ºC to improve the quality of

562 the voltage clamp, (28). To reduce the amplitude of the sodium channel currents, 50 mM Na$^+$ was

563 present in the intracellular solution: 70 Cs-gluconate, 30 Na-gluconate, 10 TEA-Cl, 5 4-AP, 10 EGTA,

564 1 CaCl$_2$, 10 HEPES, 4 Mg-ATP, 0.3 Na$_3$-GTP, 10 Na$_2$-phosphocreatine. Soluble full length tau

565 aggregates were added to intracellular solution to give a final concentration of 444 nM (20 µg/ml tau)

566 to align with the findings of this study and of (11).

567 Series resistance (R$_s$) was measured throughout the recording and were typically in the range of 6-12

568 MΩ. Cells with R$_s$ over 15 MΩ or those that differed by more than 20 % over the period of recording

569 were discarded. R_s was not compensated, but the liquid junction potential of ~ 8 mV was

570 corrected. Leak currents were subtracted using the P/n protocol (1/4) and the resulting data

571 displayed.

572 The stimulation protocol was adapted from (28) to allow fully clamped somatic Na$^+$ channel currents to

573 be recorded. Neurons were held at -80 mV. A depolarising pre-pulse was given (5 ms, -40 mV) to

574 activate axonal, but not somatic, sodium channels. This was followed by a 1 ms step to -55 mV and

575 then voltage steps (from -60 to 60 mV, 5 ms duration) were used to elicit controlled Na$^+$ channel

576 current responses. The inter-sweep interval was 2 s. From the current responses, plots of current vs

577 voltage or conductance vs voltage were calculated.

578

579 Conductance is given by the following equation:

$$Conductance\ (g) = \frac{I_{Na}}{V_{Step} - V_{Reversal}} \qquad Eq.\ 9$$

580

581

582

583 The plot of conductance vs voltage was fitted with a Boltzmann equation:

$$y = \frac{A_1 - A_2}{1 + e^{(x-x_0)/dx}} + A_2 \qquad Eq.\ 10$$

584 and then the half activation voltage and rate of activation constant were extracted and compared

585 between control and oTau introduced neurons.

586

587 **Hodgkin Huxley action potential model**

588 The Hodgkin-Huxley (HH; 28) model is a simple but robust method for modelling the ionic

589 conductance's that generate nerve APs. The HH model can be applied to study voltage gated sodium

590 and potassium channels. It proposes that each sodium channel contains a set of 3 identical, rapidly

591 responding, activation gates (the m-gates), and a single, slower-responding, inactivation gate (the h-

592 gate) (29).

593

594 The membrane current is given by:

$$I = C_m \frac{dVm}{dt} + g_K(V_m - V_k) + g_{Na}(V_m - V_{Na}) + g_l(V_m - V_l) \qquad Eq.\ 11$$

595 Where I is the total membrane current and C_m is the membrane capacitance, g_K, g_{Na} and g_l are the

596 potassium, sodium and leak conductance's per unit area, and V_k, V_{Na} and V_l are reversal potentials.

597

598 The sodium conductance can be given by:

$$I_{Na}(t) = \bar{g}_{Na}m(V_m)^3 h(V_m)(V_m - E_{Na}) \qquad Eq.\ 12$$

599 Where $\bar{g}_{Na}$ is the maximal sodium conductance and *m* and *h* are quantities between 0 and 1 that are

600 associated with sodium channel activation and inactivation, respectively. V_m is the membrane

601 potential and E_{Na} is the reversal potential for sodium.

602

603 Initial parameters were assigned as follows: $\bar{g}_{Na}: 120\ mS/cm^2$, $\bar{g}_K: 36\ mS/cm^2$, $g_l: 0.3\ mS/cm^2$,

604 $C_m: 1\ \mu F/cm^2$, $Vm: -70\ mV$, $E_{Na}: 60\ mV$, $E_K: -88\ mV$, $E_l: -54.4\ mV$ in line with (29). All modelling

605 was completed using either MATLAB or Julia software platforms (53).

606

607 **Statistics and reproducibility**

16

608 We have compared each of the aggregated tau truncations with FL-oTau and with control. We have
609 illustrated the induced-changes to neuronal properties in the manuscript using normalised data
610 (although all statistical analysis was carried out on the non-normalised data) as we are interested in
611 the change over time (from 0 mins; whole-cell breakthrough). Data was normalized to time zero when
612 the tau constructs will not have had time to diffuse into the recorded cell, this acts as an internal
613 control. Therefore normalising the data to the values at whole-cell breathrough makes it easier to
614 observe any changes that occur over time and compare this between conditions.

615

616 Due to small sample sizes (n < 15), statistical analysis was performed using non-parametric methods
617 on the non-normalised data: Kruskal–Wallis analysis of variance (ANOVA), Mann Whitney and
618 Wilcoxon signed-rank tests as required for non-parametric data. All data is represented as mean and
619 standard error of the mean with individual experiments represented by single data points. No post-
620 hoc corrections have been made following these comparisons. There is considerable controversy
621 surrounding the arbitrariness and subjectivity that can be introduced into the presentation of the
622 results by the number of post-hoc comparisons that could or could not be undertaken (54–56). We
623 therefore prefer to present the results directly from the raw tests on a case-by-case basis. Each
624 recorded cell is one data point. All experimental conditions were measured using multiple animals,
625 only 1 cell was recorded per slice and recording conditions were interleaved to remove bias
626 introduced from individual animals. Data points for each experimental condition were derived from a
627 minimum of 4 individual animals.

628

629 A further direct comparison of all the tau constructs and control samples alongside one another is
630 given in supplementary material. This is illustrated with both normalised and non-normalised data and
631 a full statistical analysis of all of the conditions relative to one on other for each parameter
632 (Supplementary Figures 1-6 and and Supplementary Tables 1-10).

633

634 **Data availability**
635 Source data underlying main figures are presented in Supplementary Data 1. All other data that
636 support the findings of this study are available within the article and its Supplementary Material or are
637 available from the corresponding author upon reasonable request.

638

639

17

670 **Competing interests:**
671 The authors declare no competing interests.
672

673 **References**
674

675 1. Brandt R, Lee G. Functional organization of microtubule-associated protein tau. Identification
676 of regions which affect microtubule growth, nucleation, and bundle formation in vitro. J Biol
677 Chem. 1993 Feb 15;268(5):3414–9.
678 2. Tracy TE, Gan L. Tau-mediated synaptic and neuronal dysfunction in neurodegenerative
679 disease. Curr Opin Neurobiol. 2018 Aug;51:134–8.
680 3. Dickson DW, Kouri N, Murray ME, Josephs KA. Neuropathology of frontotemporal lobar
681 degeneration-tau (FTLD-tau). J Mol Neurosci MN. 2011 Nov;45(3):384–9.
682 4. Rademakers R, Neumann M, Mackenzie IR. Advances in understanding the molecular basis
683 of frontotemporal dementia. Nat Rev Neurol. 2012 Aug;8(8):423–34.
684 5. Köpke E, Tung YC, Shaikh S, Alonso AC, Iqbal K, Grundke-Iqbal I. Microtubule-associated
685 protein tau. Abnormal phosphorylation of a non-paired helical filament pool in Alzheimer
686 disease. J Biol Chem. 1993 Nov 15;268(32):24374–84.
687 6. Avila J, Santa-María I, Pérez M, Hernández F, Moreno F. Tau phosphorylation, aggregation,
688 and cell toxicity. J Biomed Biotechnol. 2006;2006(3):74539.

689   7.   Maeda S, Sahara N, Saito Y, Murayama S, Ikai A, Takashima A. Increased levels of granular
690   tau oligomers: an early sign of brain aging and Alzheimer's disease. Neurosci Res. 2006
691   Mar;54(3):197–201.
692   8.   Andorfer C, Kress Y, Espinoza M, de Silva R, Tucker KL, Barde Y-A, et al.
693   Hyperphosphorylation and aggregation of tau in mice expressing normal human tau isoforms.
694   J Neurochem. 2003 Aug;86(3):582–90.
695   9.   Cowan CM, Chee F, Shepherd D, Mudher A. Disruption of neuronal function by soluble
696   hyperphosphorylated tau in a Drosophila model of tauopathy. Biochem Soc Trans. 2010
697   Apr;38(2):564–70.
698   10. Yoshiyama Y, Higuchi M, Zhang B, Huang S-M, Iwata N, Saido TC, et al. Synapse loss and
699   microglial activation precede tangles in a P301S tauopathy mouse model. Neuron. 2007 Feb
700   1;53(3):337–51.
701   11. Hill E, Karikari TK, Moffat KG, Richardson MJE, Wall MJ. Introduction of Tau Oligomers into
702   Cortical Neurons Alters Action Potential Dynamics and Disrupts Synaptic Transmission and
703   Plasticity. eneuro. 2019 Sep;6(5):ENEURO.0166-19.2019.
704   12. Hoover BR, Reed MN, Su J, Penrod RD, Kotilinek LA, Grant MK, et al. Tau mislocalization to
705   dendritic spines mediates synaptic dysfunction independently of neurodegeneration. Neuron.
706   2010 Dec 22;68(6):1067–81.
707   13. Mondragón-Rodríguez S, Salas-Gallardo A, González-Pereyra P, Macías M, Ordaz B, Peña-
708   Ortega F, et al. Phosphorylation of Tau protein correlates with changes in hippocampal theta
709   oscillations and reduces hippocampal excitability in Alzheimer's model. J Biol Chem. 2018
710   Jun 1;293(22):8462–72.
711   14. Puzzo D, Piacentini R, Fá M, Gulisano W, Li Puma DD, Staniszewski A, et al. LTP and
712   memory impairment caused by extracellular Aβ and Tau oligomers is APP-dependent. eLife.
713   2017 Jul 11;6.
714   15. Acquarone E, Argyrousi EK, van den Berg M, Gulisano W, Fà M, Staniszewski A, et al.
715   Synaptic and memory dysfunction induced by tau oligomers is rescued by up-regulation of the
716   nitric oxide cascade. Mol Neurodegener. 2019 Jun 27;14(1):26.
717   16. Fá M, Puzzo D, Piacentini R, Staniszewski A, Zhang H, Baltrons MA, et al. Extracellular Tau
718   Oligomers Produce An Immediate Impairment of LTP and Memory. Sci Rep. 2016 Jan
719   20;6:19393.
720   17. Ondrejcak T, Klyubin I, Corbett GT, Fraser G, Hong W, Mably AJ, et al. Cellular Prion Protein
721   Mediates the Disruption of Hippocampal Synaptic Plasticity by Soluble Tau In Vivo. J
722   Neurosci Off J Soc Neurosci. 2018 Dec 12;38(50):10595–606.
723   18. Hill E, Wall MJ, Moffat KG, Karikari TK. Understanding the Pathophysiological Actions of Tau
724   Oligomers: A Critical Review of Current Electrophysiological Approaches. Front Mol Neurosci
725   [Internet]. 2020 [cited 2021 Jan 20];13. Available from:
726   https://www.frontiersin.org/articles/10.3389/fnmol.2020.00155/full
727   19. Hill E, Gowers R, Richardson MJE, Wall MJ. α-Synuclein Aggregates Increase the
728   Conductance of Substantia Nigra Dopamine Neurons, an Effect Partly Reversed by the KATP

19

729   Channel Inhibitor Glibenclamide. eNeuro [Internet]. 2021 Jan 1 [cited 2021 Jan 20];8(1).

730   Available from: https://www.eneuro.org/content/8/1/ENEURO.0330-20.2020

731 20. Kaufmann TJ, Harrison PM, Richardson MJE, Pinheiro TJT, Wall MJ. Intracellular soluble α-

732   synuclein oligomers reduce pyramidal cell excitability. J Physiol. 2016 May 15;594(10):2751–

733   72.

734 21. Cicognola C, Brinkmalm G, Wahlgren J, Portelius E, Gobom J, Cullen NC, et al. Novel tau

735   fragments in cerebrospinal fluid: relation to tangle pathology and cognitive decline in

736   Alzheimer's disease. Acta Neuropathol (Berl). 2019 Feb;137(2):279–96.

737 22. Karikari TK, Nagel DA, Grainger A, Clarke-Bland C, Hill EJ, Moffat KG. Preparation of stable

738   tau oligomers for cellular and biochemical studies. Anal Biochem. 2019 Feb 1;566:67–74.

739 23. Karikari TK, Nagel DA, Grainger A, Clarke-Bland C, Crowe J, Hill EJ, et al. Distinct

740   Conformations, Aggregation and Cellular Internalization of Different Tau Strains. Front Cell

741   Neurosci [Internet]. 2019 [cited 2021 Jan 20];13. Available from:

742   https://www.frontiersin.org/articles/10.3389/fncel.2019.00296/full

743 24. Lapointe NE, Horowitz PM, Guillozet-Bongaarts AL, Silva A, Andreadis A, Binder LI. Tau 6D

744   and 6P isoforms inhibit polymerization of full-length tau in vitro. Biochemistry. 2009 Dec

745   29;48(51):12290–7.

746 25. Badel L, Lefort S, Berger TK, Petersen CCH, Gerstner W, Richardson MJE. Extracting non-

747   linear integrate-and-fire models from experimental data using dynamic I–V curves. Biol

748   Cybern. 2008 Nov;99(4–5):361–70.

749 26. Badel L, Lefort S, Brette R, Petersen CCH, Gerstner W, Richardson MJE. Dynamic *I-V*

750   Curves Are Reliable Predictors of Naturalistic Pyramidal-Neuron Voltage Traces. J

751   Neurophysiol. 2008 Feb;99(2):656–66.

752 27. Harrison PM, Badel L, Wall MJ, Richardson MJE. Experimentally Verified Parameter Sets for

753   Modelling Heterogeneous Neocortical Pyramidal-Cell Populations. Sporns O, editor. PLOS

754   Comput Biol. 2015 Aug 20;11(8):e1004165.

755 28. Milescu LS, Bean BP, Smith JC. Isolation of somatic Na+ currents by selective inactivation of

756   axonal channels with a voltage prepulse. J Neurosci Off J Soc Neurosci. 2010 Jun

757   2;30(22):7740–8.

758 29. Hodgkin AL, Huxley AF. A quantitative description of membrane current and its application to

759   conduction and excitation in nerve. J Physiol. 1952 Aug 28;117(4):500–44.

760 30. Braak H, Braak E. Neuropathological stageing of Alzheimer-related changes. Acta

761   Neuropathol (Berl). 1991;82(4):239–59.

762 31. Zhou L, McInnes J, Wierda K, Holt M, Herrmann AG, Jackson RJ, et al. Tau association with

763   synaptic vesicles causes presynaptic dysfunction. Nat Commun. 2017 May 11;8:15295.

764 32. Tamagnini F, Walsh DA, Brown JT, Bondulich MK, Hanger DP, Randall AD. Hippocampal

765   neurophysiology is modified by a disease-associated C-terminal fragment of tau protein.

766   Neurobiol Aging. 2017 Dec;60:44–56.

767 33. Fourcaud-Trocmé N, Hansel D, Vreeswijk C van, Brunel N. How Spike Generation
768   Mechanisms Determine the Neuronal Response to Fluctuating Inputs. J Neurosci. 2003 Dec
769   17;23(37):11628–40.

770 34. Rall W, Segev I. Space-Clamp Problems When Voltage Clamping Branched Neurons With
771   Intracellular Microelectrodes. In: Smith TG, Lecar H, Redman SJ, Gage PW, editors. Voltage
772   and Patch Clamping with Microelectrodes [Internet]. New York, NY: Springer; 1985 [cited
773   2021 Feb 9]. p. 191–215. Available from: https://doi.org/10.1007/978-1-4614-7601-6_9

774 35. Spruston N, Jaffe DB, Williams SH, Johnston D. Voltage- and space-clamp errors associated
775   with the measurement of electrotonically remote synaptic events. J Neurophysiol. 1993 Aug
776   1;70(2):781–802.

777 36. Castelli L, Biella G, Toselli M, Magistretti J. Resurgent Na+ current in pyramidal neurones of
778   rat perirhinal cortex: axonal location of channels and contribution to depolarizing drive during
779   repetitive firing. J Physiol. 2007;582(3):1179–93.

780 37. Kole MHP, Ilschner SU, Kampa BM, Williams SR, Ruben PC, Stuart GJ. Action potential
781   generation requires a high sodium channel density in the axon initial segment. Nat Neurosci.
782   2008 Feb;11(2):178–86.

783 38. Royeck M, Horstmann M-T, Remy S, Reitze M, Yaari Y, Beck H. Role of Axonal NaV1.6
784   Sodium Channels in Action Potential Initiation of CA1 Pyramidal Neurons. J Neurophysiol.
785   2008 Oct 1;100(4):2361–80.

786 39. Stuart G, Schiller J, Sakmann B. Action potential initiation and propagation in rat neocortical
787   pyramidal neurons. J Physiol. 1997;505(3):617–32.

788 40. Puopolo M, Raviola E, Bean BP. Roles of Subthreshold Calcium Current and Sodium Current
789   in Spontaneous Firing of Mouse Midbrain Dopamine Neurons. J Neurosci. 2007 Jan
790   17;27(3):645–56.

791 41. de Lera Ruiz M, Kraus RL. Voltage-Gated Sodium Channels: Structure, Function,
792   Pharmacology, and Clinical Indications. J Med Chem. 2015 Sep 24;58(18):7093–118.

793 42. Akin EJ, Solé L, Dib-Hajj SD, Waxman SG, Tamkun MM. Preferential Targeting of Nav1.6
794   Voltage-Gated Na+ Channels to the Axon Initial Segment during Development. PLoS ONE.
795   2015 Apr 15;10(4). Available from: https://www.ncbi.nlm.nih.gov/pmc/articles/PMC4398423/

796 43. Garrido JJ, Giraud P, Carlier E, Fernandes F, Moussif A, Fache M-P, et al. A targeting motif
797   involved in sodium channel clustering at the axonal initial segment. Science. 2003 Jun
798   27;300(5628):2091–4.

799 44. Van Wart A, Trimmer JS, Matthews G. Polarized distribution of ion channels within
800   microdomains of the axon initial segment. J Comp Neurol. 2007 Jan 10;500(2):339–52.

801 45. Lorincz A, Nusser Z. Molecular Identity of Dendritic Voltage-Gated Sodium Channels.
802   Science. 2010 May 14;328(5980):906–9.

803 46. Catterall WA. Voltage-gated sodium channels at 60: structure, function and pathophysiology.
804   J Physiol. 2012 Jun 1;590(Pt 11):2577–89.

805 47. Patino GA, Isom LL. Electrophysiology and beyond: Multiple roles of Na+ channel β subunits
806   in development and disease. Neurosci Lett. 2010 Dec 10;486(2):53–9.

807   48.   Kontis KJ, Rounaghi A, Goldin AL. Sodium Channel Activation Gating Is Affected by
808   Substitutions of Voltage Sensor Positive Charges in All Four Domains. J Gen Physiol. 1997
809   Oct 1;110(4):391–401.

810   49.   Fozzard HA, Sheets MF, Hanck D. The Sodium Channel as a Target for Local Anesthetic
811   Drugs. Front Pharmacol [Internet]. 2011 [cited 2021 Feb 9];2. Available from:
812   https://www.frontiersin.org/articles/10.3389/fphar.2011.00068/full

813   50.   Bezanilla F. The Voltage Sensor in Voltage-Dependent Ion Channels. Physiol Rev. 2000 Jan
814   4;80(2):555–92.

815   51.   Karikari TK, Keeling S, Hill E, Lantero Rodríguez J, Nagel DA, Becker B, et al. Extensive
816   Plasmid Library to Prepare Tau Protein Variants and Study Their Functional Biochemistry.
817   ACS Chem Neurosci. 2020 Oct 7;11(19):3117–29.

818   52.   Uhlenbeck GE, Ornstein LS. On the Theory of the Brownian Motion. Phys Rev. 1930 Sep
819   1;36(5):823–41.

820   53.   Bezanson J, Edelman A, Karpinski S, Shah VB. Julia: A Fresh Approach to Numerical
821   Computing. SIAM Rev. 2017 Jan 1;59(1):65–98.

822   54.   Rothman K J. No adjustments are needed for multiple comparisons. Epidemiology.
823   1990;1(1):43–6.

824   55.   Saville D J. Basic statistics and the inconsistency of multiple comparison procedures. J Exp
825   Psychol Can Psychol Expérimentale. 2003;57(3):167–75.

826   56.   Stewart-Oaten A. Rules and Judgments in Statistics: Three Examples. Ecology.
827   1995;76(6):2001–9.

828

829

830

831

832   **Figure 1: Structure and characterisation of the tau truncations.**

833   **a)** Schematic illustration of the recombinant tau constructs used in this study. Full length (FL) tau
834   (441) has two N terminal repeat sequences (N1, N2) and four microtubule-binding pseudorepeat
835   domains (R1–R4). Two trunctions were tested. The first, is an N-terminal truncated form of FL tau
836   (termed C^{FRAG}) which consists of amino acids 124-444. The second, is the N-terminal fragment that is
837   removed by the C^{FRAG} truncation (termed N^{FRAG}) which consists of amino acids 1-123, including both
838   of the N-terminal repeat sequences. **b)** All three versions of tau (FL, C^{FRAG} and N^{FRAG}) were visualised
839   as monomers, and after undergoing the oligomerisation protocol. Overnight incubation at room
840   temperature in the absence of any aggregation inducer (*e.g.*, heparin) allowed each protein variant to
841   form small, soluble tau aggregates, as monitored by negative-stain transmission electron microscopy.
842   While FL and C^{FRAG} both formed granular oligomer-like aggregates, the N-terminal fragment
843   polymerized into amorphous structures with no consistent shape. Insets: Regions at higher
844   magnification to illustrate aggregate shape. The monomer preparations did not form any visible
845   aggregates. Scale bars = 200 nm and insets 20 nm.

846   **Figure 2**: **The effects of FL-oTau on input resistance and action potential waveform are**
847   **abolished by N-terminal truncation, although the effects on firing rate remain.**

848   **a)** Standard current−voltage responses for control neurons (grey; *n*=12 cells, 8 animals) in which
849   vehicle was injected, for neurons in which FL oTau was introduced (red; *n*=12 cells, 8 animals) and for
850   neurons where C^{FRAG} oTau (blue; *n*=12 cells, 7 animals) was introduced. The responses are shown
851   over the 40-minute recording period. There were no significant changes with control neurons to any of
852   the measured parameters (0 vs 40 mins, peak input resistance *p* = 0.1455, firing rate *p* = 0.1831,
853   action potential amplitude *p* = 0.0732 or action potential width *p* = 0.2266). However, there were clear
854   changes to neuronal properties in the response to FL oTau and C^{FRAG} oTau. Panels **b, c, f, g** and **h**
855   display both average data (mean ± SEM) as well as inidividual data points for each condition over
856   time. **b)** Graph plotting resting membrane potential against time. There was no change over the
857   period of recording for any of the three experimental conditions (0 vs 40 mins; vehicle *p* = 0.0898, FL
858   oTau and C^{FRAG} oTau, p = 0.0898, 0.0859 and 0.0801 respectively). **c)** Graph plotting input against
859   time. FL-oTau significantly increased input resistance resistance (at 40 mins, input resistance was
860   increased to 130 ± 6.3 % of the value at time 0, whole cell breakthrough, *p* = 0.0005) whereas C^{FRAG}-
861   oTau had no effect (at 40 mins, the input resistance was 100 ± 2.1 % of the value at time 0, *p* =
862   0.9263). **d)** Example action potential (AP) waveforms for the three experimental conditions recorded
863   at time 0 (whole cell breakthrough) and after 40 minutes. Neither vehicle nor C^{FRAG}-oTau had any
864   effect on the action potential waveform. FL oTau reduced the height (amplitude measured at the peak
865   relative to baseline) and increased the width of the AP. **e)** Example membrane-potential responses to
866   naturalistic current injection at time 0 (after whole-cell breakthrough) and after 40 min of recording for
867   each of the three conditions (vehicle, FL-oTau and C^{FRAG}-oTau). For FL oTau, there was a reduction
868   in action potential height coupled with an increase in the firing rate. C^{FRAG} -oTau had no effect on
869   action potential height but did significantly increase the firing rate. Vehicle had no effect. **f)** Graph
870   plotting normalised firing rate (normalised to time 0) against time. Both FL and C^{FRAG} tau oligomers

871   produce a significant increase in firing rate (FL oTau: at 40 mins, the firing rate measured from the

872   voltage response to naturalistic current injection, was 171 ± 19.3 % of that at time 0, p = 0.02; C^{FRAG}

873   oTau: at 40 mins, the firing rate was 164 ± 22.5 % of that at time 0, p = 0.0132). No change was

874   observed with vehicle. **g)** Graph plotting action potential height against time and **(h)** action potential

875   width against time. A reduction in action potential amplitude and increase in action potential width are

876   produced by FL oTau (action potential amplitude at 40 minutes significantly (p= 0.001) reduced to 70

877   ± 7.4 % of that at time 0 minutes and action potential width at 40 minutes significantly (p = 0.0352)

878   increased to 134 ± 17.2 % of that at time 0 minutes) but not by C^{FRAG} oTau (action potential amplitude

879   at 40 minutes 91 ± 1.6 % of that at time 0 minutes, p= 0.0791 or action potential width at 40 minutes

880   102 ± 3.0 % of that at time 0 minutes p = 0.4746). Error bars represent standard error of the mean

881   (SEM).

882

883   **Figure 3: FL oTau and C^{FRAG} oTau reduce the rheobase (minimum current required to fire an**

884   **action potential).**

885   In the same recordings that are illustrated in Figure 2, the rheobase current (minimal current to evoke

886   an AP) was determined by injecting a current ramp (-50 pA to 200 pA) and measuring the minimum

887   current required to fire an action potential. **a)** Example voltage responses to ramp current injections in

888   control (vehicle) neurons where FL-oTau was injected and neurons where C^{FRAG} oTau was

889   introduced. The voltage responses are shown at zero minutes (whole cell breakthrough) and after 40

890   minutes of recording (the traces are superimposed). There was no change in control recordings

891   (vehicle) but there is a clear negative shift (reduction in current required to fire an action potential) for

892   both tau species. **b)** Graph plotting the mean rheobase current for control (vehicle), FL and C^{FRAG} tau

893   oligomers against time (mean ± SEM) and the corresponding individual data points. There was no

894   significant difference in rheobase in control, FL or C^{FRAG} neurons at time 0 (whole-cell breakthrough)

895   using a Kruskal-Wallis One-Way ANOVA (at 0 mins, the mean rheobase in control was 61 ± 3.47 pA,

896   with FL the mean rheobase was 68 ± 5.39 pA and with C^{FRAG} the mean rheobase was 79 ± 7.74 pA, p

897   = 0.1289). In control neurons, there was no significant difference in the rheobase current over the

898   duration of the recording (at 40 minutes, the rheobase was 105 ± 3 % of the value at time 0 mins,

899   p=0.0830, Table 1). However, both FL and C^{FRAG} tau oligomers significantly reduced the current

900   needed to elicit an action potential. For FL oTau, at 40 minutes the rheobase was 66 ± 7 % of the

901   value at time 0 mins (p = 0.0015). When C^{FRAG} tau was introduced, at 40 minutes the rheobase was

902   70 ± 5 % of the value at time 0 mins (p = 0.0005, Table 1). Error bars represent standard error of the

903   mean (SEM).

904
905
906
907
908
909
910   **Figure 4: oTau-mediated hyperpolarising shift in spike initiation threshold.**

24

911 For the dynamic I-V protocol, a naturalistic current is injected into the cell and the recorded voltage is
912 then used to extract a set of parameters (resting potential E, time constant τ, and spike-threshold
913 voltage VT; see methods for more details). The second point where the DIV curve crosses 0 mV/ms is
914 the spike initiation threshold. **a)** Representative examples of dynamic IV curves, for a neuron with the
915 N-terminal truncation of tau (C^{FRAG}-oTau) introduced, generated at 0 mins (green) and after 40 mins
916 (pink). A hyperpolarising shift in spike initiation threshold of 4 mV (more negative) can be observed
917 (circles on the graph). Panels **b** and **c** display both average data (mean ± SEM) as well as inidividual
918 data points for each condition over time. **b)** The mean normalised spike threshold data (to value at
919 time 0) is plotted against time. There was no significant difference between the spike initiation
920 threshold in control vs C^{FRAG} neurons at time 0 (whole-cell breakthrough), thus the recordings were
921 comparable (mean threshold in control neurons was -53.82 ± 1.46 mV, n = 12 cells, compared to the
922 mean threshold in C^{FRAG} neurons which was -53.7 ± 1.64 mV, n = 12 cells, p = 0.5185). In control
923 neurons, there was no significant difference in spike threshold over the duration of the recording (at
924 40 minutes, the spike threshold was 101.3 ± 1.1 % of the value at time 0 mins, p = 0.4766). Whereas
925 for neurons where C^{FRAG} was introduced, the spike initiation threshold was significantly reduced (more
926 negative) at 40 minutes was compared to 0 minutes (at 40 minutes, the spike threshold was 94.5 ±
927 0.9 % of the value at time 0 mins, p = 0.0010). **c)** Graph plotting spike onset against time. There was
928 no significant difference between the onset in control vs C^{FRAG} neurons at time 0 (whole-cell
929 breakthrough), thus the recordings were comparable in quality and stability (mean spike onset in
930 control neurons was 1.01 ± 0.09 mV, n = 12 cells, compared to the mean threshold in C^{FRAG} neurons
931 which was 0.98 ± 0.13 mV, n = 12 cells, p = 0.1285). In control neurons, there was no significant
932 difference in spike onset over the duration of the recording (at 40 minutes, the spike onset was 103.2
933 ± 5.7 % of the value at time 0 mins, p = 0.9102). Whereas for neurons where 444 nM aggregated
934 C^{FRAG} tau was introduced, the onset was increased (steeper, reflecting increased excitability) at 40
935 minutes was compared to 0 minutes (at 40 minutes, the spike onset was 140.4 ± 8.2 % of the value at
936 time 0 mins, p = 0.0015). The increase in spike onset observed in neurons where C^{FRAG}-oTau was
937 introduced reflects faster spike generation after threshold was reached. **d)** Membrane potential
938 responses to naturalistic current injection for the neuron analysed in **(a)** demonstrates an increase in
939 firing rate mediated by the introduction of C^{FRAG} tau oligomers. **e)** Simulated (refractory integrate and
940 fire model) membrane potential responses produced from the extracted neuronal parameters at time
941 0 mins (green). The firing rate in the simulational is a good match to what was measured
942 experimentally. The spike threshold was shifted by -4 mV and the simulation re-run (blue). The
943 increase in firing rate was comparable to the experimental data at 40 mins **(d)**. The same procedure
944 was performed, but only with a shift in the spike onset. This had little effect on the firing rate, thus
945 confirming that the increase in firing rate is predominantly mediated by a shift in spike threshold. Error
946 bars represent standard error of the mean (SEM).
947
948
949

25

950 **Figure 5: The rapid increase in input resistance mediated by N^{FRAG-}tau (444 nM) is due to**
951 **aggregation in the soma impeding current flow.**

952 **a)** Representative examples of voltage responses to ramp current injection and voltage responses to
953 step current injections at 0 mins (whole cell breakthrough) and after 5 mins for neurons with N^{FRAG}-tau
954 (444 nM) injected. N^{FRAG}-tau rapidly induces a large increase in input resistance and a reduction in
955 spike height. At 5 minutes, the input resistance was 169 ± 24.2 % of that at 0 minutes (whole cell
956 breakthrough), the time constant was reduced to 77 ± 3.2 % of that at 0 minutes and this change in
957 time constant reflected a change in whole-cell capacitance (by 5 minutes the capacitance was
958 reduced to 53 ± 5.4 % of that at 0 minutes (n = 4 cells, 4 animals). **b)** Bright-field image of a
959 hippocampal CA1 pyramidal neuron showing two patch pipettes simultaneously recording from the
960 soma. In this example pipette 1 was used to inject current and record the voltage response whereas
961 pipette 2 was used only for recording the voltage responses. **c)** Schematic of the stimulation protocol.
962 A 200 pA hyperpolarising current step was injected via pipette 1. and the voltage response was
963 recorded from both pipettes (1. and 2.). **d)** An example experiment where both pipettes contained
964 vehicle. There was no change in the relative amplitude of the voltage responses between 0 mins
965 (whole-cell breakthrough) and 5 minutes for pipette 1 and pipette 2 (the relative response was 97 ±
966 1.7 % of the response at 0 minutes, p = 0.1484, n = 8 cells, 4 animals). **e)** An example experiment
967 where 444 nM N^{FRAG}-tau was introduced via pipette 1. There is a clear increase in the voltage
968 response measured in pipette 1 as a result of an increase in input resistance. However, there is no
969 increase in the voltage response in pipette 2. Thus, the relative ratio of voltage responses between
970 the two pipettes has fallen, indicative of impeded current flow in the soma. (at 5 minutes the relative
971 response was 58.4 ± 7 % of the response at 0 minutes, p = 0.0078, n = 8 cells, 4 animals). **f)** Graph
972 plotting the mean normalised ratio of voltage responses (pipette 2/ pipette 1) for recordings where
973 both pipettes contained vehicle (control, n = 8 cells) and when pipette 1 contained 444 nM N^{FRAG}-tau
974 (n = 8 cells). There is a significant reduction in the ratio of voltage responses when 444 nM N^{FRAG}-tau
975 is injected, suggesting that less current reaches pipette 2. Error bars represent standard error of the
976 mean (SEM).

977

978 **Figure 6: The effects of FL-oTau on action-potential waveform are reproduced by lower**
979 **concentrations of N^{FRAG}-tau aggregates and monomers.**

980 Panels **a, b, c, d, f** and **g** display both average data (mean ± SEM) as well as inidividual data points
981 for each condition over time. **a)** Graph showing that there is no change to the resting membrane
982 potential over the period of recording for any of the conditions (133 nM N^{FRAG}-tau monomers or
983 aggregates; N^{FRAG} tau aggregates: at 40 mins, the resting membrane potential was 99 ± 1.0 % of that
984 at time 0, p = 0.9609, n = 12 cells, 7 animals; N^{FRAG} tau monomers at 40 mins, the resting membrane
985 potential was 104 ± 2.4 % of that at time 0, p = 0.0938, n=12 cells, 6 animals. **b)** Graph showing that
986 there is no change to the input resistance over the period of recording for 133 nM N^{FRAG}-tau
987 aggregates or monomers (N^{FRAG} tau aggregates: at 40 mins, the peak input resistance, measured
988 from the voltage response to step current injection, was 102 ± 7.7 % of that at time 0, p = 0.9531;

26

989   N^{FRAG} tau monomers: at 40 mins, the peak input resistance, measured from the voltage response to

990   step current injection, was 102 ± 4.1 % of that at time 0, *p* = 0.9395. **c)** Graph showing that there is no

991   change to the firing rate over the period of recording for 133 nM N^{FRAG} aggregates or monomers

992   (N^{FRAG} tau aggregates: at 40 mins, the firing rate, measured from the voltage response to naturalistic

993   current injection, was 107 ± 13.6 % of that at time 0, *p* = 0.7471; N^{FRAG} tau monomers: at 40 mins, the

994   firing rate, measured from the voltage response to naturalistic current injection, was 106 ± 10.5 % of

995   that at time 0, *p* = 0.5068). **d)** Graph showing that there is no change to the rheobase current (minimal

996   current to evoke an AP) over the period of recording for 133 nM N^{FRAG}-tau aggregates or monomers

997   (N^{FRAG} tau aggregates: at 40 mins, the rheobase was 127 ± 11.9 % of that at time 0, *p* = 0.1294;

998   N^{FRAG} tau monomers: at 40 mins, the rheobase was 116 ± 10.1 % of that at time 0, *p* = 0.2402). **e)**

999   Representative examples of average action potential waveforms from neurons with either 444 nM FL-

1000   oTau, 133 nM N^{FRAG}-tau aggregates or 133 nM N^{FRAG}-tau monomers introduced. In all 3 conditions

1001   there is a comparable decrease in action potential height and increase in action potential width. **f)**

1002   Graph plotting mean normalised action potential height (at time 0) against time. There is a

1003   comparable decrease in action potential height for 133 nM N^{FRAG}-tau aggregates, monomers and FL-

1004   oTau (N^{FRAG} tau aggregates: action potential amplitude at 40 minutes was significantly reduced to 76

1005   ± 2.9 % of that at time 0 minutes, *p*=0.0005; N^{FRAG} tau monomers: action potential amplitude at 40

1006   minutes was significantly reduced to 82 ± 2.6 % of that at time 0 minutes, *p*=0.0010). **g)** Graph

1007   plotting mean normalised action potential width (at time 0) against time. There is a comparable

1008   increase in action potential width over the period of recording for 133 nM N^{FRAG}-tau aggregates,

1009   monomers and FL-oTau (N^{FRAG} tau aggregates: action potential width at 40 minutes was significantly

1010   increased to 118 ± 7.4 % of that at time 0 minutes, *p* = 0.0186; N^{FRAG} tau 32 monomers: action

1011   potential width at 40 minutes was significantly increased to 123 ± 2.0 % of that at time 0 minutes, *p* =

1012   0.0303). Pale red lines demonstrate the effects of FL-oTau for comparison (data presented in figure

1013   2). Action potential (AP), Firing rate (FR), Input resistance (Rin), Resting membrane potential (resting

1014   membrane potential). Error bars represent standard error of the mean (SEM).

1015

1016   **Figure 7: FL tau oligomers directly modify somatic sodium channel currents recorded from**

1017   **hippocampal CA1 neurons in acute slices. a)** Example of the recording protocol (adapted from 27).

1018   A pre-pulse step of 5 ms from (-80 mV to -40 mV) elicits a current response from axonal (but not

1019   somatic) sodium channels. There is a brief step to -55 mV (1 ms) before the steps that are used to

1020   evoke the controlled sodium channel currents (15 ms in duration). The steps were given consecutively

1021   from -60 V to + 60 mV (5 mV increment) with a 2 s gap between each sweep. Leak currents were

1022   subtracted with the P/N protocol (1/4) and the junction potential (+ 8 mV) was corrected for. **b)** In

1023   order to look at the full range of of the changes that had been observed with the different truncations,

1024   FL-oTau (444 nM) was used in these experiments and compared against control. Conductance was

1025   calculated using the following equation: conductance *(g) = current (I)/ (Vstep −Vreversal).* The

1026   conductance in response to steps up to 0 mV is plotted as a mean (and SEM) for all control cells

1027   (vehicle, *n*=7 cells, 6 animals). **c)** The conductance in response to steps up to 0 mV is plotted as a

1028   mean (and SEM) for all cell where FL-oTau (444 nM) was introduced (*n* = 7 cells, 5 animals) is

1029 plotted. For B and C, the grey line is 0 mins and the red 20 mins. A Boltzmann fit allows half activation

1030 voltage and the time constant (measure of the speed of activation). **d)** Mean change in half activation

1031 from 0 mins to 20 mins for control and FL-oTau injected neurons. Data is given relative to the value at

1032 time 0. Mean and SEM are shown, and individual data points are overlaid on top. While control

1033 (vehicle) cells are stable over time (at 20 mins, the half activation was 98 ± 1.0 % of that at time 0, p =

1034 0.2031), Fl-oTau introduced cells show a significant decrease in half activation (activate at lower

1035 voltages; increase in excitability; at 20 minutes, the half activation was 150 ± 11.7 % of that at time 0,

1036 p = 0.0078), but they also show a doubling of the activation constant (**e**; in control cells, at 20 mins, it

1037 was 101 ± 3.6 % of that at time 0, p = 0.9375, whereas in FL-oTau introduced neurons had increased

1038 significantly to 171 ± 15.4 % of that at time 0, p = 0.0078), fitting with the slower rise time of APs

1039 observed in (11). **f, g)** Example sodium currents from neurons with vehicle introduced (control) and

1040 FL-oTau introduced at 0 mins and after 20 mins demonstrating the reduction in peak current induced

1041 by FL-oTau, with no change introduced in control. **h, i)** Raw conductance data (averaged) to highlight

1042 the reduction in maximal conductance for FL-oTau after 20 mins. Inset demonstrates the crossover at

1043 low voltages, where FL- oTau at 20 mins produces a higher conductance, despite the maximal

1044 conductance being reduced at higher voltages. **j)** A simple Hodgkin Huxley model of action-potential

1045 dynamics was used to predict the effect of reducing the maximal sodium channel conductance on the

1046 action potential waveform. Reducing the maximal sodium channel conductance by two thirds, as

1047 measured experimentally in **(i)** produced similar changes in the action potential waveform **(j)** to that

1048 observed experimentally with FL-oTau **(k)**. Error bars represent standard error of the mean (SEM).

Parameter	Vehicle/ control (n = 12)				Full length tau (n = 12)				C^{FRAG} (n = 12)			
	0 mins		40 mins		0 mins		40 mins		0 mins		40 mins	
	Mean	SEM	Mean	SEM	Mean	SEM	Mean	SD	Mean	SEM	Mean	SEM
RMP (mV)	-64	± 1.07	-66	± 1.36	-66	± 0.75	-64	± 1.30	-64	± 0.92	-67	± 1.52
Input Resistance (MΩ)	204	± 18.6	197	± 20.1	165	± 6.29	218	± 16.1	178	± 13.4	177	± 11.7
Firing Rate (Hz)	1.73	± 0.4	1.63	± 0.45	1.25	± 0.3	1.73	± 0.3	1.1	± 0.19	1.5	± 0.21
AP Height (mV)	85	± 2.52	83	± 2.86	87	± 3.42	63	± 7.48	89	± 2.19	86	± 2.45
AP width (ms)	1.8	± 0.09	1.7	± 0.08	1.8	± 0.05	2.4	± 0.34	1.8	± 0.06	1.9	± 0.06
Rheobase (pA)	61	± 3.47	60	± 4.51	68	± 5.39	47	± 7.42	79	± 7.74	56	± 8.18

1049

1050 **Table 1: Electrophysiological parameters measured for CA1 neurons with either vehicle, C^{FRAG} or N^{FRAG} introduced.** Recordings were made from
1051 hippocampal CA1 neurons. There was no significant difference between any of the measured parameters at 0 minutes (whole-cell breakthrough), using
1052 Kruskal Wallis ANOVAs (see text for p values). Comparisons were then made between 0 and 40 minutes for each of the conditions using non-parametric
1053 Wilcoxon-signed rank tests (see text for p values). Data shown as mean and SEM. Action potential (AP), Firing rate (FR), Input resistance (IR), Resting
1054 membrane potential (RMP).

29

1055
1056

Parameters	FL-oTau (444 nM)	C^{FRAG}-oTau (444 nM)	N^{FRAG}-oTau (444 nM)	N^{FRAG}-oTau (133 nM)	N^{FRAG}-Tau (133 nM)	Potential mechanism
AP height	↓	-	↓	↓	↓	Slower activation of voltage-gated sodium channels
AP width	↑	-	↑	↑	↑	
Input resistance	↑	-	↑	-	-	Aggregation in the soma impeding current flow, artificially altering capacitance.
Firing rate	↑	↑	-	-	-	Shift in spike initiation threshold (more hyperpolarised). Shift in the half activation of voltage-gated sodium channels
Rheobase	↓	↓	-	-	-	

1057

1058 Table 2: Summary of findings using recombinant truncations of tau and the
1059 identified mechanisms.
1060

1061

1062

1063

1064

1065

1066

1067

1068

1069

1070

1071

1072

1073

1074

a

Full length tau (FL)

1   444

N | N1 | N2 | | | | R1 | R2 | R3 | R4 | | C

N-terminal fragment (N^FRAG)

1   123

N | N1 | N2 |

C-terminal fragment (C^FRAG)

124   444

| | | R1 | R2 | R3 | R4 | | C

b

FL   C^FRAG   N^FRAG

Oligomers
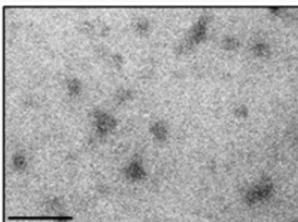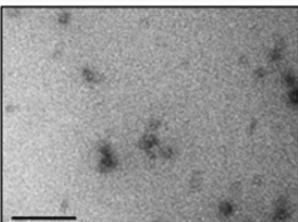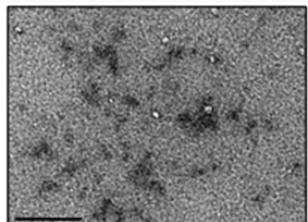
Monomers

a

Control

FL-oTau

C^{FRAG}-oTau

0 mins
40 mins

20 mV
0.2 s

b
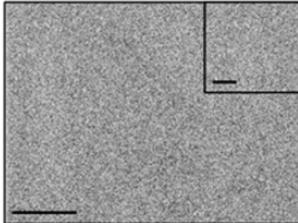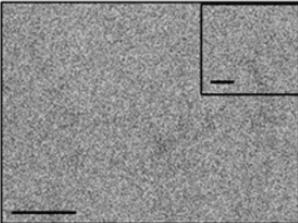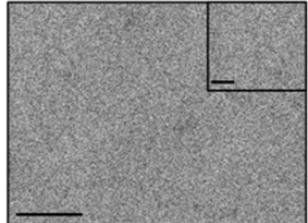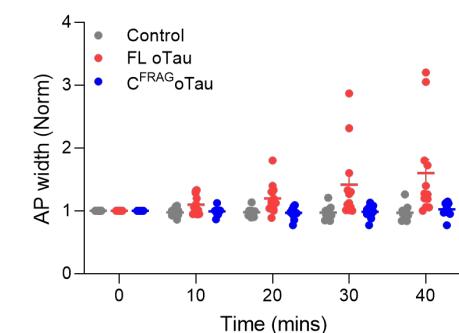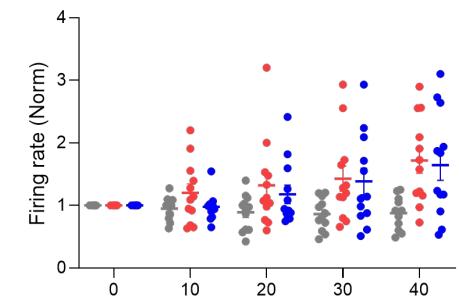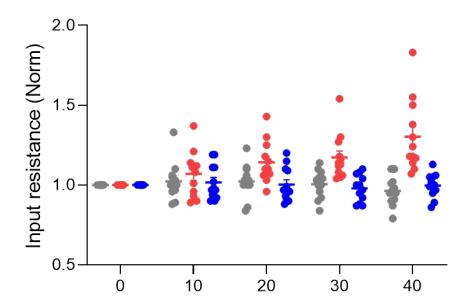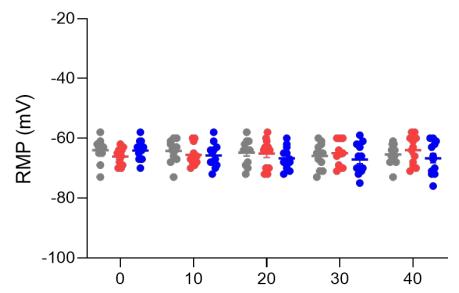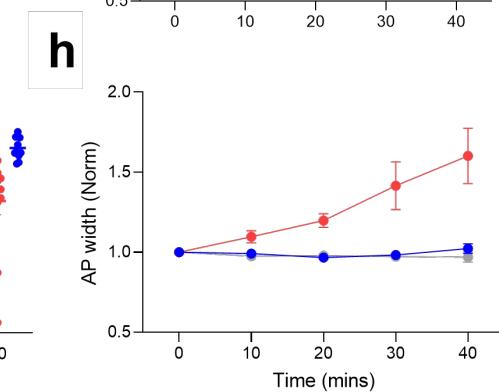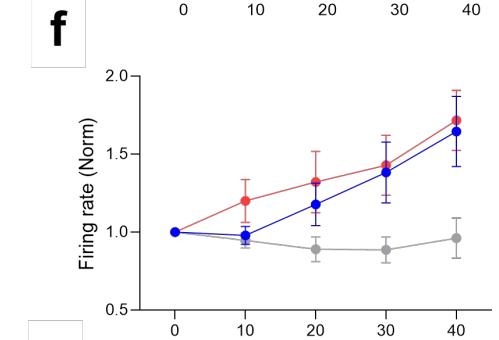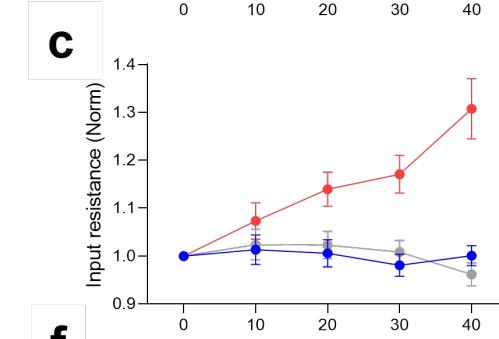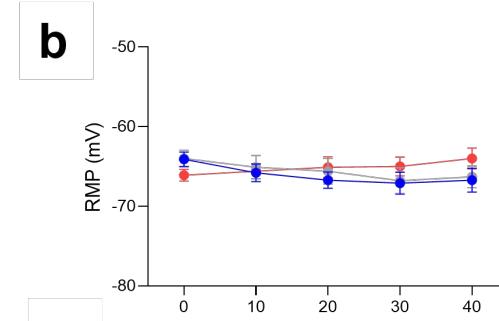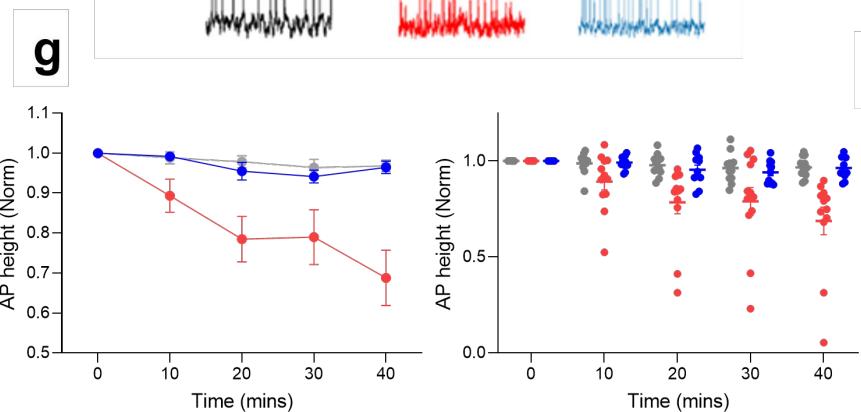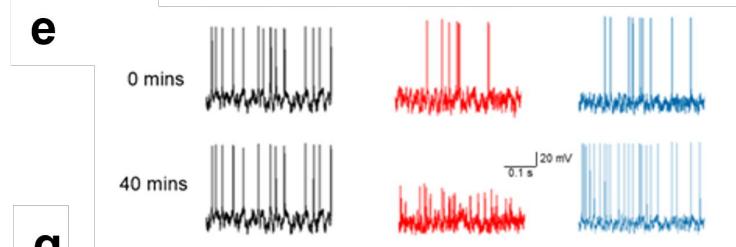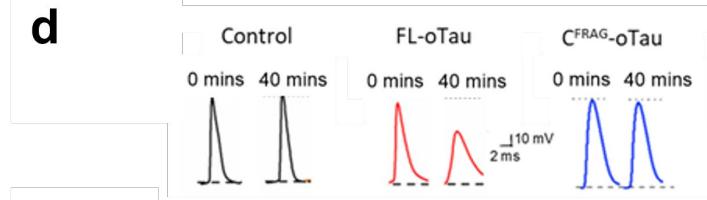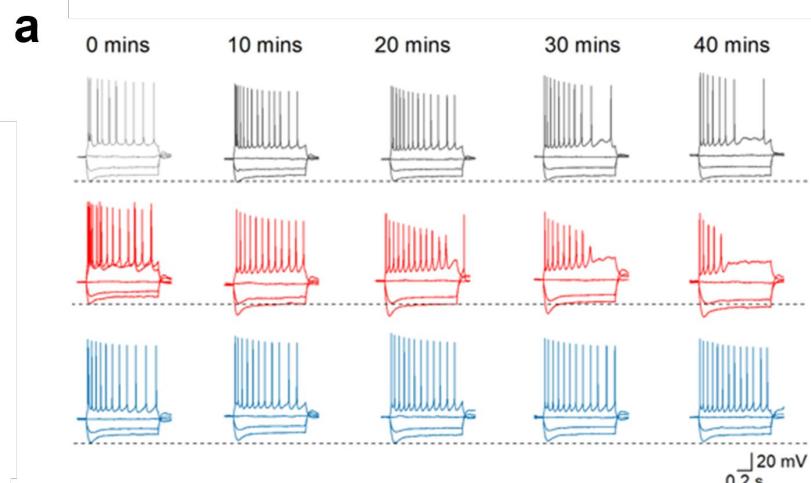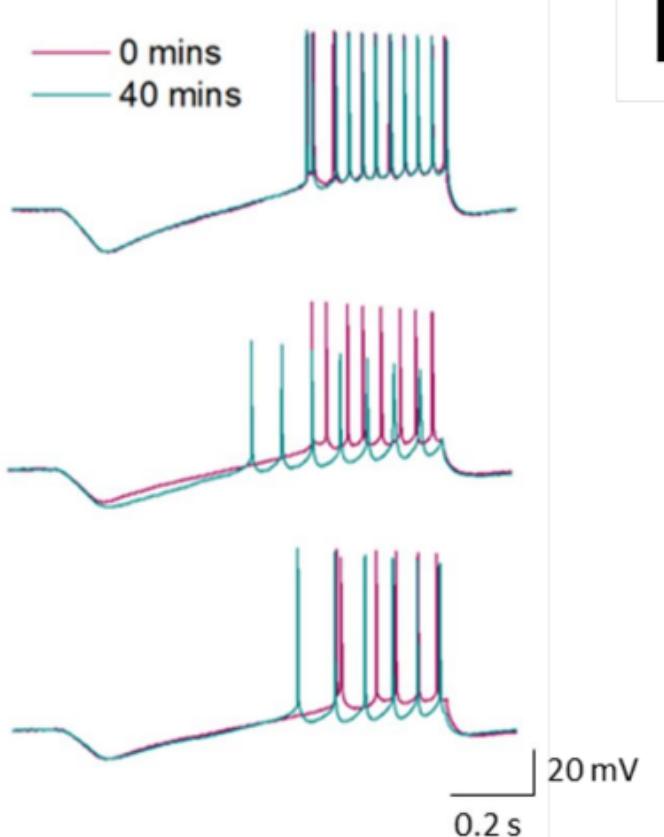
Control
FL-oTau
C^{FRAG}-oTAU

Rheobase current (Norm)

Time (mins)

Control
FL oTau
C^{FRAG} oTAU

Rheobase current (Norm)

Time (mins)

a

F(V) (mv/ms) vs Voltage (mV)

- 40 mins
- 0 mins
- ○ spike threshold

b

Threshold (Norm) vs Time (mins)
- C^{FRAG} -oTAU
- Control

c

Spike Onset (Norm) vs Time (mins)
- C^{FRAG} -oTAU
- Control

d

Experimental traces

0 mins, 1.1 Hz   40 mins, 2.3 Hz

e

Simulated traces

0 mins, 1.2 Hz   0 mins (V$_T$ shifted) 2.3 Hz

0 mins, 1.2 Hz   0 mins (DT shifted) 1.1 Hz

20 mV
10 s

a

0 mins   5 mins

20 mV
0.2 s

b

1. Inj & rec

2. Rec

c

Pipette 1. Inject current | 200 pA

Pipette 1. Record voltage

Pipette 2. Record voltage

10 mV
0.5 s

d

0 mins   5 mins

1. vehicle

2. vehicle

1.   2.

e

0 mins   5 mins

1. N^{FRAG}-tau

2. vehicle

1.   2.

TAU

10 mV
0.5 s

f

Control

N^{FRAG} tau aggregates

Normalised $V_{rec}/V_{inj/rec}$

time (secs)

a

-40 mV

-80 mV

1 ms

5 ms   15 ms

500 pA

- 60 mV
- 55 mV
- 50 mV
- 45 mV
- 40 mV
- 35 mV
- 30 mV
- 25 mV
- 20 mV
- 15 mV
- 10 mV
- 5 mV

b Control

mean normalised conductance

■ 0 mins ● 20 mins
Boltzmann 0 mins
Boltzmann 20 mins

voltage (step to; mV)

c Tau

voltage (step to; mV)

d

ΔHalf activation

control   tau

e

ΔRate constant

control   tau

f

control 0 mins   control 20 mins

g

tau 0 mins   tau 20 mins

500 pA
2 ms

h Control

mean raw conductance (nS)

■ 0 mins ● 20 mins

voltage (step to; mV)

i Tau

voltage (step to; mV)

j Simulated

1/3 sodium conductance

20 mV
2.5 s

k Experimental

oTau 0 min   oTau 40 min

10 mV
2.5 ms